

# We are IntechOpen, the world's leading publisher of Open Access books Built by scientists, for scientists

6,900

Open access books available

185,000

International authors and editors

200M

Downloads

Our authors are among the

154

Countries delivered to

TOP 1%

most cited scientists

12.2%

Contributors from top 500 universities



WEB OF SCIENCE™

Selection of our books indexed in the Book Citation Index  
in Web of Science™ Core Collection (BKCI)

Interested in publishing with us?  
Contact [book.department@intechopen.com](mailto:book.department@intechopen.com)

Numbers displayed above are based on latest data collected.  
For more information visit [www.intechopen.com](http://www.intechopen.com)



# Novel Magnetic-Sensing Modalities with Nitrogen-Vacancy Centers in Diamond

*Huijie Zheng, Arne Wickenbrock, Georgios Chatzidrosos, Lykourgos Bougas, Nathan Leefer, Samer Afach, Andrey Jarmola, Victor M. Acosta, Jingyan Xu, Geoffrey Z. Iwata, Till Lenz, Zhiyin Sun, Chen Zhang, Takeshi Ohshima, Hitoshi Sumiya, Kazuo Nakamura, Junichi Isoya, Jörg Wrachtrup and Dmitry Budker*

## Abstract

In modern-day quantum metrology, quantum sensors are widely employed to detect weak magnetic fields or nanoscale signals. Quantum devices, exploiting quantum coherence, are inevitably connected to physical constants and can achieve accuracy, repeatability, and precision approaching fundamental limits. As a result, these sensors have shown utility in a wide range of research domains spanning both science and technology. A rapidly emerging quantum sensing platform employs atomic-scale defects in crystals. In particular, magnetometry using nitrogen-vacancy (NV) color centers in diamond has garnered increasing interest. NV systems possess a combination of remarkable properties, optical addressability, long coherence times, and biocompatibility. Sensors based on NV centers excel in spatial resolution and magnetic sensitivity. These diamond-based sensors promise comparable combination of high spatial resolution and magnetic sensitivity without cryogenic operation. The above properties of NV magnetometers promise increasingly integrated quantum measurement technology, as a result, they have been extensively developed with various protocols and find use in numerous applications spanning materials characterization, nuclear magnetic resonance (NMR), condensed matter physics, paleomagnetism, neuroscience and living systems biology, and industrial vector magnetometry. In this chapter, NV centers are explored for magnetic sensing in a number of contexts. In general, we introduce novel regimes for magnetic-field probes with NV ensembles. Specifically, NV centers are developed for sensitive magnetometers for applications where microwaves (MWs) are prohibitively invasive and operations need to be carried out under zero ambient magnetic field. The primary goal of our discussion is to improve the utility of these NV center-based magnetometers.

**Keywords:** NV center, novel magnetometry

## 1. Introduction

### 1.1 Microwave-free magnetometry

The negatively-charged NV center in diamond, an atomic-scale defect consisting of a substitutional nitrogen adjacent to a vacancy in the diamond lattice, has emerged as a unique nanoscale sensor with numerous interesting applications in the past years and has been extensively explored which yields various technological breakthroughs. It can be used, based on employing electron spin resonance (ESR) techniques, to detect magnetic fields [1], temperature [2, 3], electric fields [4], strain [5], rotation [6, 7], and other fundamental physical quantity, for example, quantum geometrical phases [8]. In particular, the NV center in diamond has been proved to be a successful magnetic-field sensor by using the technique optically-detected magnetic resonance (ODMR) [9], for both with single and ensembles of NV centers [1, 10, 11]. The ODMR sensing protocols are typically realized by polarizing the NV electron spin with green light and manipulating the spin state with MW fields. An optical readout step involves either detection of NV-photoluminescence (PL) [1] or absorption of 1042 nm radiation resonant with the singlet transition [12–15]. When the applied MW fields are resonant with the splitting of the magnetic sublevels in the ground state of the NV-center, the transfer of spin populations results in an observable change in PL or absorption.

The use of strong MW fields is not desirable in certain cases that it can produce interference in the measurement environment which is detrimental to the sensing protocol and therefore limits the applications of an NV-based sensors. An example is, in the context of magnetic induction tomography, the detection of eddy currents in conductive materials [16–18], which is later demonstrated in the publication [19], where the application of MW to the diamond will be heavily affected by the presence of a conductive structure under investigation. Another example is imaging the pattern of conductive, magnetic structures [20].

There have been, in the literature, several demonstrations of MW-free, and all-optical, diamond-based magnetic measurement, which are implemented initially with single NV centers [21–23], and recently with NV ensembles [20]. These protocols have been realized by exploiting either the properties of the NV-center's PL or their decoherence properties at certain external magnetic fields. In particular, one of the main approaches exploits the properties of the NV-center PL in the strong magnetic-field regime for all-optical magnetic field mapping. The basic operating principle resides on the fact that under the application of a strong magnetic field (much stronger than any strain field within the diamond crystal), the transverse magnetic-field components induce mixing of the NV-center spin states. Note that this spin-mixing leads to modifications of the NV spin dynamics under optical illumination, yielding a reduction of the ODMR contrast, which eventually hampers ODMR-based magnetometric protocols. However, this reduction in contrast is accompanied by an overall reduction of the NV-center PL, which can be exploited in an all-optical magnetic-field sensing and imaging protocol. So far, these protocols remain either qualitative, requiring complicated setups to achieve high spatial resolution, or lack high magnetic-field sensitivities and bandwidth.

An alternative approach exploits the decoherence properties of the NV-center. The presence of high off-axis magnetic fields increases the amount of spin mixing and results in a reduction of the longitudinal spin relaxation time ( $T_1$ ) [24]. This technique has been used to image weak fluctuating magnetic fields and to characterize spin noise in ferromagnetic materials. More recently, an all-optical, MW-free, spin-relaxation contrast magnetometer for the imaging of thin magnetic films, with a temporal and spatial resolution of 20 ms and 440 nm, respectively, was realized [20].

Recently, it has been demonstrated the principles of a sensitive MW-free magnetometer by exploiting the properties of the ground-state level anticrossing of the NV center in diamond. In particular, a  $\sim 102.4$  mT background magnetic field causes degeneracy and mixing (anticrossing) of ground-state Zeeman sublevels, which is observable as a drop in the fluorescence signal. Changes in the external magnetic field will perturb the anti-crossing condition and, thus, result in a photoluminescence signal that can be monitored and used for magnetic-field measurement. This type of magnetometer offers technical and logistical advantages in bio-imaging and conductive-material sensing. Finally, the MW-free technique is deployed to perform eddy current detection. The method exhibits a combination of high spatial resolution and high sensitivity. As an example of application, detection of eddy-current induced magnetic field on metal samples, by implementing a cross-relaxation, microwave-free, magnetic detection scheme, is demonstrated. Compared to existing technologies, the demonstrated method exhibits higher, sub-millimeter spatial resolution.

A schematic of the experimental setup is shown in **Figure 1**. The diamond is placed within a custom-made electromagnet (**Figure 1(a)**) and can be rotated around the z-axis. The electromagnet can be rotated around the y-axis and also moved with a motorized 3D translation stage to align the magnetic field with the respect to the diamond. Therefore, with all the degrees of freedom, the position of

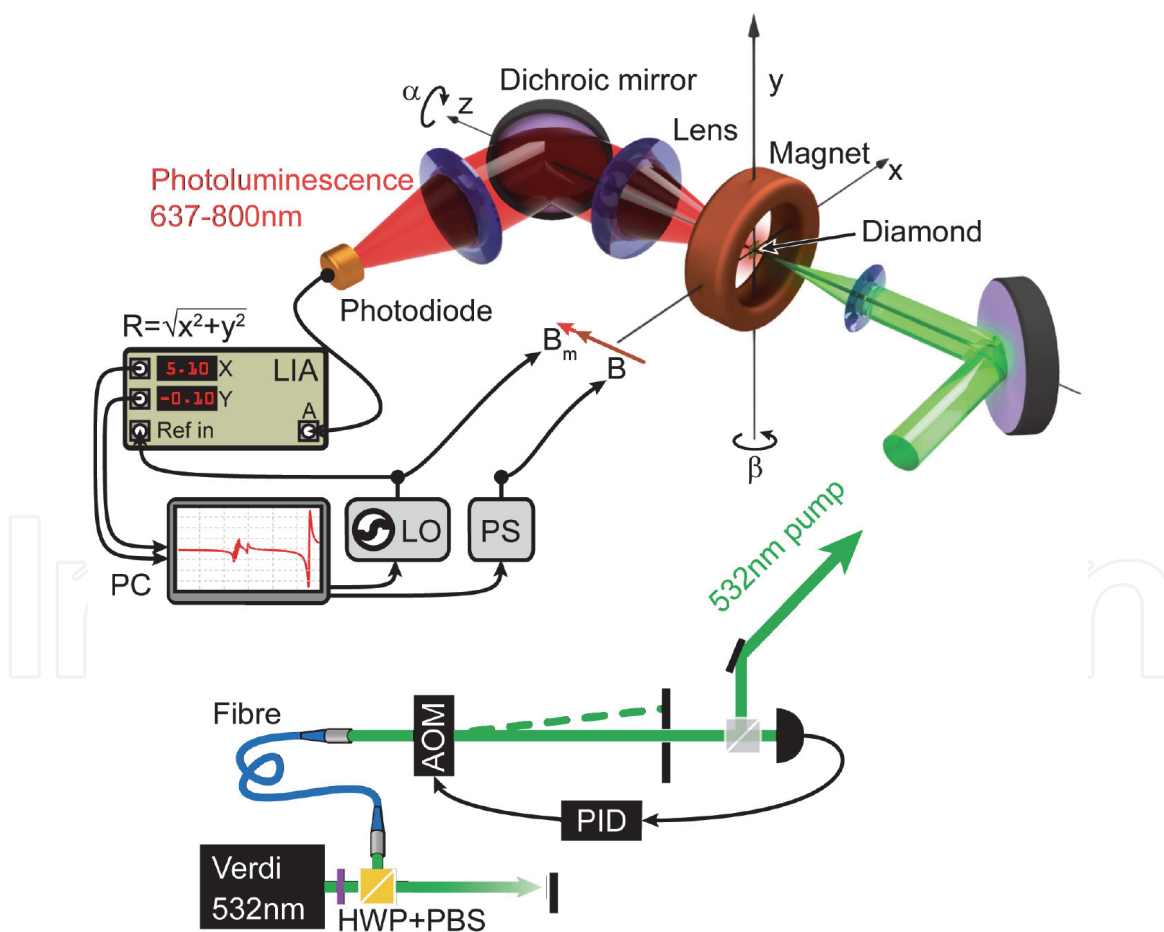


**Figure 1.** Schematic of the experimental setup. The diamond is placed within a custom-made electromagnet and can be rotated around the z-axis. The electromagnet can be moved with a computer-controlled 3D translation stage to align the magnetic field with respect to the diamond. The laser light propagates through an acousto-optical modulator, part of which is monitored on a photodetector (PD). The signal is used as a monitor/measurement signal to a PID controller to stabilize the beam power. The beam is focused with a 40 mm focal-length lens into the diamond after the acousto-optical modulator (AOM). The photoluminescence is collected with a 30 mm focal-length lens (numerical aperture  $\sim 0.5$ ) and focused onto a PD. The PD signal is sent to the lock-in amplifier (LIA). Figure adopted from Ref. [25].

diamond can be centralized in the magnet and the alignment of the [25] NV-axis to the magnetic field can be optimized.

To apply small modulation of the magnetic field, a secondary coil is wound around the diamond mount. An oscillating field  $B_m$  is produced by the coil which is also used as the local oscillator for the LIA.

The NV centers in diamond are optically spin-polarized with 532 nm laser light. Before the diamond, the light is sent through an acousto-optical modulator to enable power modulation. Part of the laser light is split-off and measured on a photodiode (PD). The signal is input into a feedback controller to stabilize the beam power. After the AOM, the beam is focused with a lens into the diamond. The red/near-infrared NV-PL is collected with a 30 mm focal-length lens, which is then separated from the green transmission with a dichroic mirror and a notch-band optical filter for the green pump light before it's being focused onto a PD. The readout signal is demodulated by the LIA at the modulating frequency or measured at DC.

The magnetic field was scanned from 0 mT to more than 110 mT after initial alignment and calibration of the magnet, and the PL was monitored. It shows the measured PL measured as a function of the applied external magnetic field in **Figure 2(a)** and the corresponding LIA signal in **Figure 2(b)**. The modulation frequency of the field was 100 kHz, the modulation amplitude was about 0.1 mT.

Both plots contain several features previously discussed in the literature. The initial gradual decrease in PL is associated with a reduction in emission of the non-aligned NV centers due to spin-mixing [27]. The observed features around 51.4 mT, correspond to cross-relaxation events between the NV center and single substitutional nitrogen (P1) centers [27–29]. Several additional features are visible. They can be associated with cross-relaxation events with either the nuclear spins of nearby P1 centers [27–29] or nuclear spins of  $^{13}\text{C}$  atoms. For details, readers can refer to Wickenbrock *et al.* [25] and Ivady *et al.* [30].

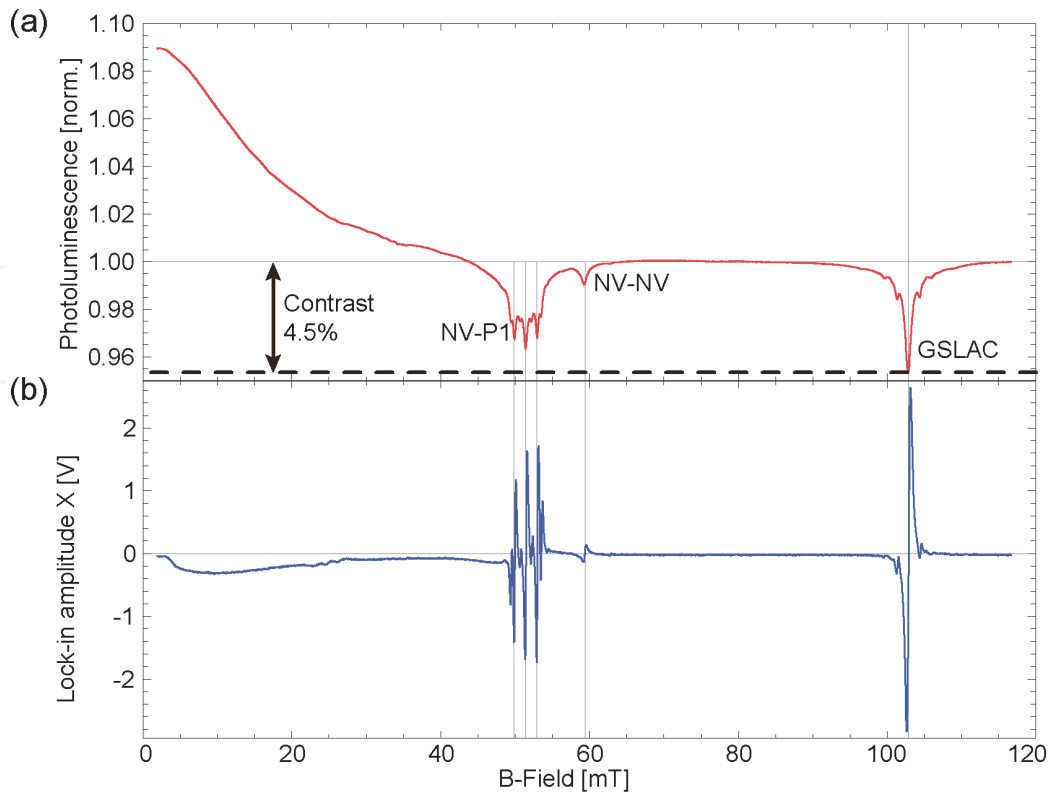


**Figure 2.**

(a) NV-PL as a function of the applied magnetic field normalized to the PL at 80 mT. (b) Derivative signal of (a) as given by the in-phase output (X) of the LIA. Figure adopted from Ref. [26].



Around the ground-state level anticrossing (GSLAC) feature, the derivative fluorescence signal as detected in the properly phased LIA X-output depends linearly on the magnetic field and can therefore be used for precise magnetic-field measurements. To subtract the coefficient for translating the LIA output signal into magnetic field value, the data within the near-linear region around the zero-crossing point are fitted with a straight line. Then the background magnetic field is set to the magnitude corresponds to the zero-crossing point where the magnetometer is maximally sensitive to external magnetic fields. At this field, the setup is insensitive to magnetic field variations and the data can be used to understand the technical noise level of the magnetometer. The noise floor is flat and around  $6 \text{ nT}/\sqrt{\text{Hz}}$  [25] (**Figure 3**).

We now discuss an application of the presented MW-free sensing technique, that is the detection of magnetic fields generated by eddy currents in conductive materials. Eddy currents are induced in conductive objects when an oscillating or pulsed magnetic field is applied. These currents in turn produce a magnetic field in

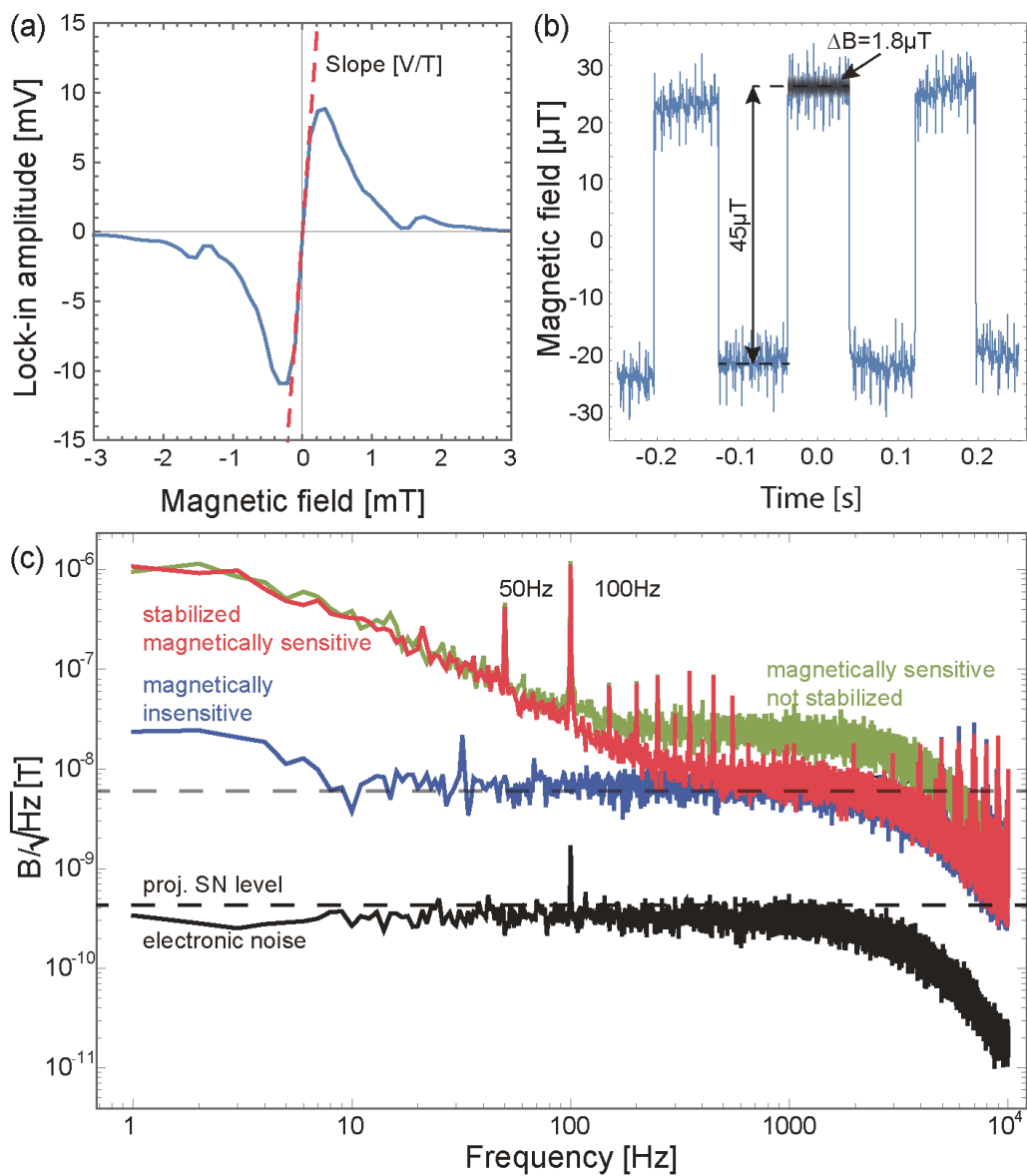


**Figure 3.** Magnetometer noise characterization. (a) Calibration data and linear fitting of the GSLAC feature around 102.4 mT. (b) Magnetic sensing validation by applying a square-wave magnetic-field. (c) Noise floor of the magnetometer: Magnetically sensitive configuration with pump laser light not stabilized (green) and stabilized (red), configuration of magnetically insensitive with pump laser light stabilized (blue) and electronic noise without the pump light stabilization (black). Figures adopted from Ref. [25].

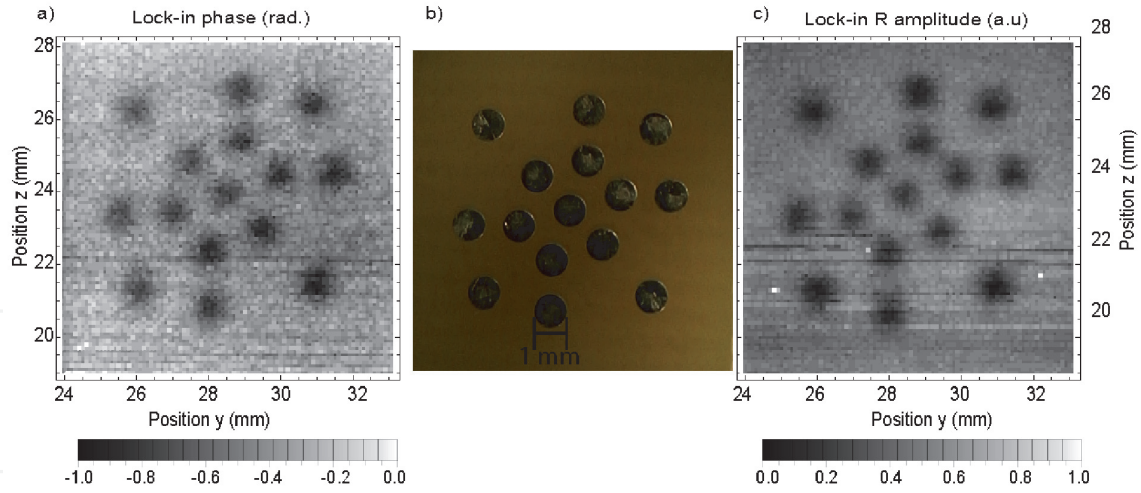


**Figure 4.**

(a), (c) Lock-in phase and lock-in R amplitude for a PCB containing fifteen aluminum dots imaged with eddy-current (b) photograph of the PCB with the corresponding length of 1 mm noted for scale. Figures adopted from Ref. [27].

response. A measurement of this field provides means to detect the eddy currents [18]. The induced field depends on the material's properties and shape, as well as the skin depth for the applied alternating field [19]. This has been demonstrated with vapor-cell magnetometers [18] and is a standard technique in industry with inductive coils. The detection of eddy currents with coils is an established technique. The benefits of using NV centers could be the high spatial resolution and the possibility to investigate highly conductive materials since the magnetometer can sense oscillating fields down to DC.

The eddy-current detection should be realized without MWs, since, because of the proximity to conducting materials, the amplitude and phase of the MWs are affected and therefore the magnetometric performance would be deteriorated. For this reason, the work was carried out with a MW-free NV magnetometer. As shown in **Figure 2**, the photoluminescence of NVs changes as the applied magnetic field increases. All the features in the plot, including the initial gradual decrease (at fields from zero to  $\approx 25$  mT), the NV-P1 feature, the NV-NV interaction feature and the GSLAC, can be utilized to probe magnetic fields. As investigated in Ref. [19], the initial gradual decrease of the NV PL is the most robust to misalignment between the applied magnetic field and the preferential NV axis among those features. Therefore, it is chosen to perform eddy current detection.

One of the advantages of NV-based sensors is their spatial resolution. For eddy-current imaging, for a constant conductivity, the smaller a material is, the smaller the amplitude of the secondary field it produces. As a test of spatial resolution, fifteen 1 mm-diameter 35  $\mu\text{m}$  thick aluminum disks are imaged. The LIA amplitude and phase affected by these disks, as response of the NV-based magnetic field sensor, is shown in **Figure 4**. The overall pattern formed by the metal disks and non-magnetic materials between them, which are both on the scale of sub-millimeter, are clearly visible.

## 2. Microwave-free vector magnetometry

Sensitive vector magnetometers are exploited in applications including magnetic navigation [31], magnetic anomaly detection [32], current and position sensing [32], and measuring biological magnetic fields [33, 34]. Several versatile

magnetometry platforms have emerged over the past decades, such as Hall probes, flux-gate, tunneling-magnetoresistance [35], SQUID based magnetometry [36] and vapor-cell-based magnetometry [37, 38]. Particularly compelling are sensors based on negatively charged NV centers in single-crystal diamond, providing high-sensitivity magnetic sensing and high-resolution imaging [15, 39, 40]. There is growing interest in magnetic-field sensors with high spatial resolution, for example to study biological processes or the composition of materials. NV magnetometry allows measuring magnetic fields at microscopic scales and/or at ambient temperature, providing new tools for probing various phenomena including semiconductor materials [41] and metallic compounds [42], magnetism in condensed matter systems [43], and elucidating spin order in magnetic materials [44].

To date, vector magnetometers based on NV diamond have been realized by interrogating ensembles of NV centers along multiple orientations [45, 46] or relying on a hybrid quantum platform involving a NV center probe and a nuclear-spin qubit at particular positions [47]. These techniques, however, are all based on ODMR technique that needs to apply microwaves simultaneously or sequentially [45, 46, 48]. The requirement of microwave control brings the possibility of spurious harmonics within the measurement and hinders applications in areas where the application of microwaves is prohibitively invasive and where it is inherently difficult to achieve such control. Although NV magnetometers have been implemented as vector magnetic probes at room temperature, it has remained challenging to achieve vector capability under cryogenic temperatures (less than 4 K) due to difficulties with thermal management. Heat dissipation from microwave wires is unavoidable and causes temperature variations, restricting the sensors for numerous innovative applications [49].

The work Zheng *et al.* [50] proposes and demonstrates a protocol that enables vectorial measurement of magnetic fields by interrogating an ensemble of NV centers aligned along only a single crystallographic axis at the GSLAC. By applying two orthogonal alternating fields, parallel and perpendicular to the chosen axis, the presented technique offers simultaneous and direct readout of full vector magnetic information, free from systematic errors during reconstruction. In contrast to existing approaches, this protocol does not employ microwave fields. Thus it is possible to extend NV-based vector magnetic sensing techniques to cryogenic temperatures.

The proposed vector magnetic sensing protocol is based on optical detection of the GSLAC of NV center in diamond. It was first proposed and demonstrated for scalar magnetometry in Wickenbrock *et al.* [25]. However, both the longitudinal and transverse magnetic fields can lead to a change in the photoluminescence signal at the GSLAC. While the response to the direction of the transverse component is non-trivial [51, 52], achieving vectorial sensing of magnetic fields with a single NV center or an ensembles along a single crystallographic axis faces a number of significant challenges.

The NV center has a spin-triplet ground state ( $S = 1$ ), which can be optically polarized to  $|m_s = 0\rangle$  and read out owing to a spin-dependent intersystem crossing into intermediate singlet states. At zero field, the  $|m_s = \pm 1\rangle$  states are (nearly) degenerate; however, these states lie higher in energy than the  $|m_s = 0\rangle$  state due to spin-spin interaction. This is the zero-field splitting  $\mathcal{D}_{gs}$  and corresponds to a frequency difference of 2.87 GHz. Because of Zeeman effect, a subset of NV centers' magnetic sublevels experience a complex GSLAC at an field  $B_z \approx 102.4$  mT [25, 53]. The energy levels, including the coupling to the intrinsic nuclear spin of nitrogen ( $I=1$ ), of the NV center are shown in **Figure 5(a)**.

**Figure 5(b)** shows the photoluminescence spectrum as a function of the external magnetic field. The GSLAC appears as a remarkably sharp feature around 102.4



mT, zoomed-in in the inset. In the inset, the visible satellite features can be attributed to cross-relaxation with the nearby spin bath [13, 25, 27, 28]. The  $|m_s = 0\rangle$  and  $|m_s = -1\rangle$  magnetic-sublevel can be coupled/mixed by transverse fields and therefore the profile of the GSLAC feature are affected which changes the contrast and amplitude. **Figure 5(c)** shows the traces of the GSLAC feature for several transverse fields in the range of  $\pm 0.06$  mT. The amplitudes of the GSLAC feature as a function of transverse field is indicated by the trace-colored dots and connected with the black line. In summary, the GSLAC contrast exhibits a relatively narrow (FWHM  $\approx 38 \mu\text{T}$ ) magnetic-resonance feature as a function of transverse magnetic field centered around zero transverse field.

To adapt a scalar magnetometer for vector measurement, it is typical to apply orthogonal fields modulated at various frequencies. Thus it is possible to determine the components along each direction by individually demodulating the signal [38]. The authors propose a method to realize vector-field sensing in the  $x$ - $y$  plane using a transverse field rotating around the  $z$ -axis with just one frequency.

To gain an intuitive understanding, the PL lineshape is approximated as a function of transverse magnetic fields with a 2-D Lorentzian centered around  $B_x = B_y = 0$ , **Figure 6(a)** (i). With a transverse field applied that is rotating around  $z$ , the PL signal will be reduced but remains unmodulated, indicated by the red curve in **Figure 6(a)** (ii). In the presence of an additional static transverse field, the PL signal shows a modulation at the rotation frequency with a minimum when the rotating field points in the same direction as the field under interrogation and a maximum when both are antiparallel, shown in **Figure 6(a)** (iii), (iv) and (v). The difference between the PL signals with (red curve) and without (blue curve)

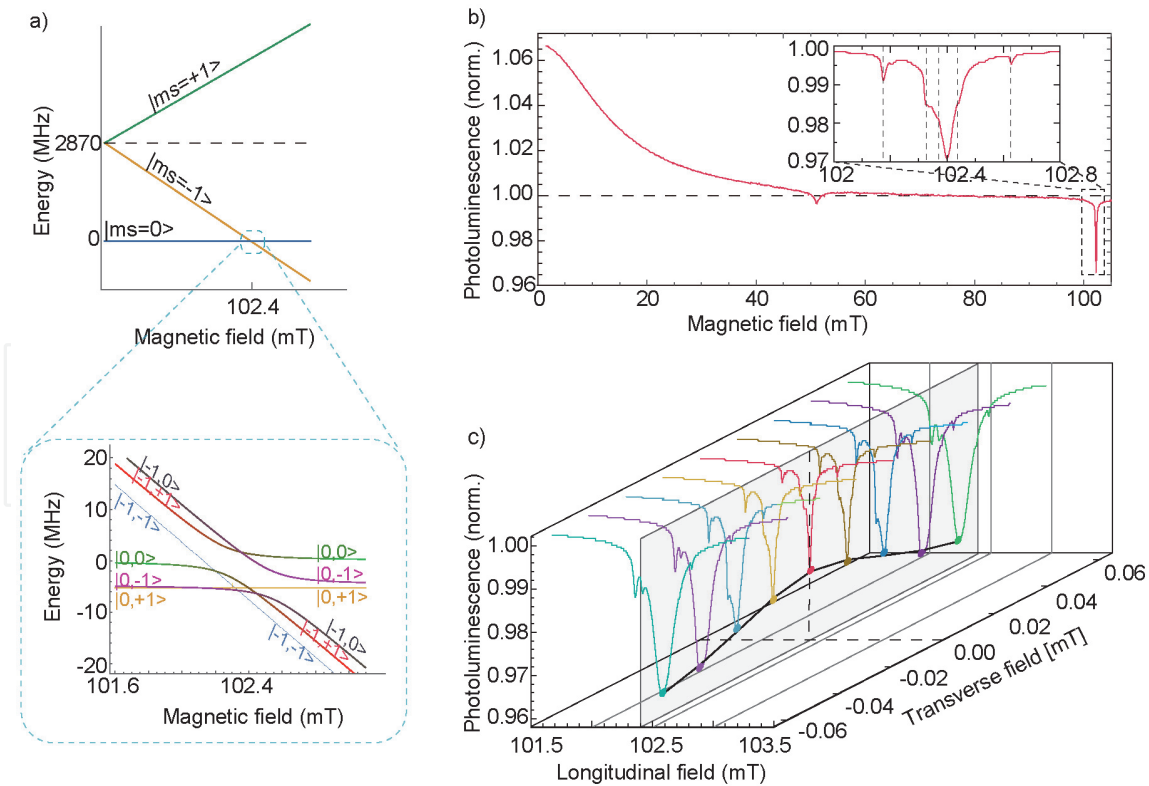


**Figure 5.**

(a) The NV ground-state energy level scheme as a function of the applied axial field. Depending on the degree of mixing, the energy levels either cross or do not cross, shown in detail in the inset. (b) the spectrum of photoluminescence signal as a function of external magnetic field, normalized to their respective signals at 80 mT. A detailed view around the GSLAC trace is shown in the inset. Other features are explained in the references [28, 29]. (c) PL traces around the GSLAC under various transverse fields. The amplitude of the contrast extracted from the curves is shown as a two-dimensional plot in a plane, indicated by solid dots in corresponding trace colors. Figures adopted from Ref. [53].

applied transverse field is shown in **Figure 6(b)**. This is then demodulated by a LIA which delivers the information of both the amplitude and the angle of the magnetic field to be measured, as shown in **Figure 6(c)**. The reference phase of the LIA was set so that a magnetic field along the  $x$ -axis corresponds to phase zero (and negative amplitude). The LIA output shows a maximum value at  $0^\circ$  when applying a field along  $x$ -axis, shown in **Figure 6(c)**. An applied field in any other direction leads to an oscillating PL signal with a corresponding phase. Therefore, the phase output of the LIA is the angle between the transverse field to be measured and the defined  $x$  and  $y$  axes.

All Cartesian magnetic-field components can be directly read out in real time with equal sensitivity in all directions, with the above mentioned  $x$  and  $y$  plus the previously demonstrated longitudinal magnetic field measurement [25]. Note here, that the coordinate axes in the  $x$ - $y$  plane is set by the reference phase of the LIA for the transverse-field signal demodulation while the phase for  $z$ -axis demodulation is tuned to maximize the amplitude of the response signal.

The experimental setup is based on **Figure 1** and extended with three pairs of orthogonal Helmholtz coils wound on a 3D printed mount. Sinusoidal signals for field modulations in the longitudinal and transverse directions and references for

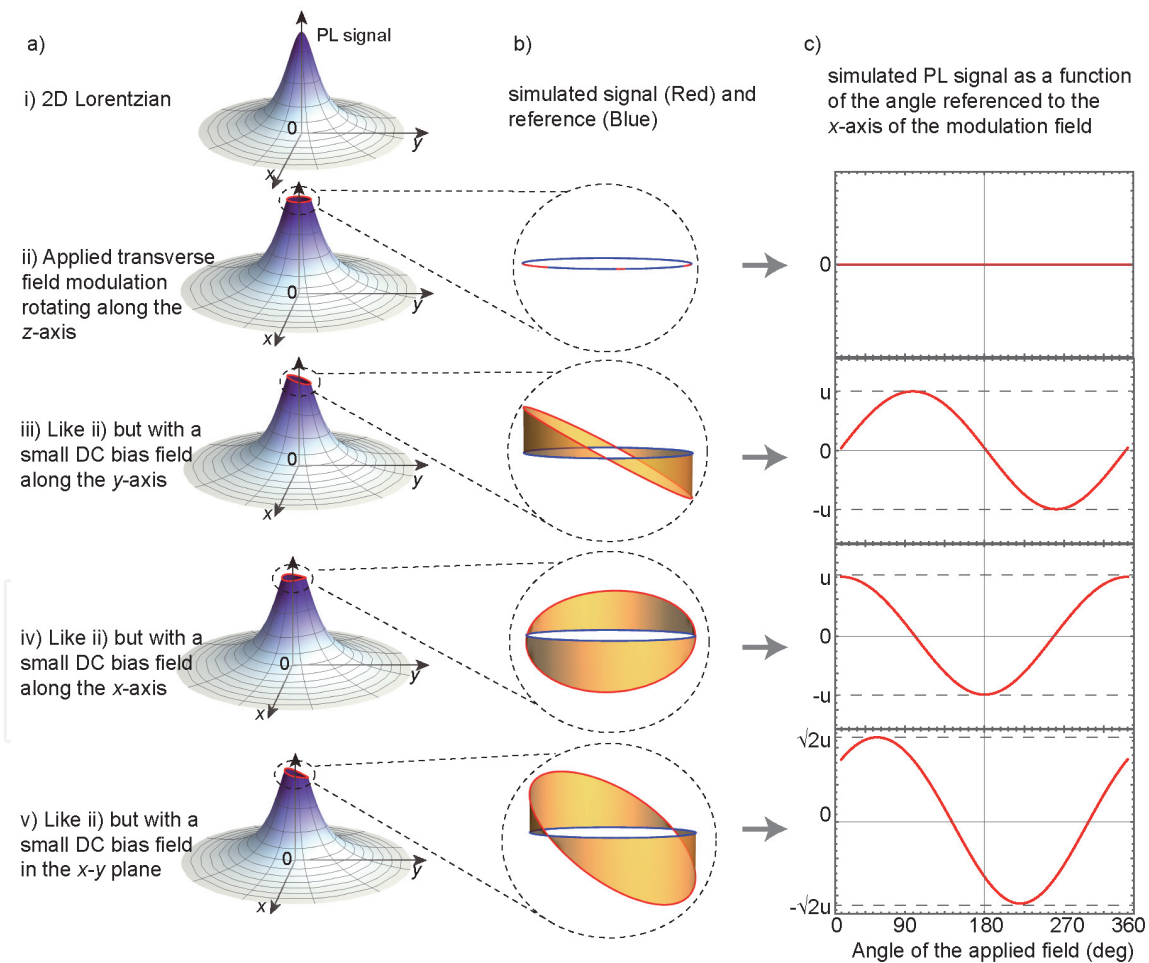


**Figure 6.** Principle of the vectorial magnetic-field sensing. (a) Simulated photoluminescence signals as a function of transverse field. The trajectories of PL signals superimposed on the 2-D Lorentzian contrast function are indicated with red curves. Figures i) to v), correspond to the following cases: i) no modulated fields and no bias fields, ii) with modulated fields but no bias fields (the time-averaged PL drops), iii) with modulated fields and bias field along  $y$ , iv) with modulated fields and bias field along  $x$ , v) with modulated fields and bias field in  $x$ - $y$  plane, respectively. (b) the subtraction of photoluminescence signals with/without presence (red curve/blue curve) of a bias field. (c) Simulated analog photoluminescence signals as a function of the angle of the modulated field referenced to the  $x$ -axis for transverse fields, flipped by  $180^\circ$  corresponding to (a) and (b). Figures adopted from Ref. [53].

the demodulation by two LIAs are provided by a two-channel function generator. One of the signals is split into two with one of them further passing through a phase shifter. These two signals are applied to two pairs of the Helmholtz coils with the same frequency but 90-degree-shifted relative phase (along the  $x$  and  $y$  axes). The Helmholtz coil pairs for the field modulation can also be used to calibrate the response to AC and DC magnetic fields  $\mathbf{B} = (B_x, B_y, B_z)$ . The applied fields, in the range of  $\pm 4 \mu\text{T}$  along each direction, are calibrated by flux gate magnetometers and

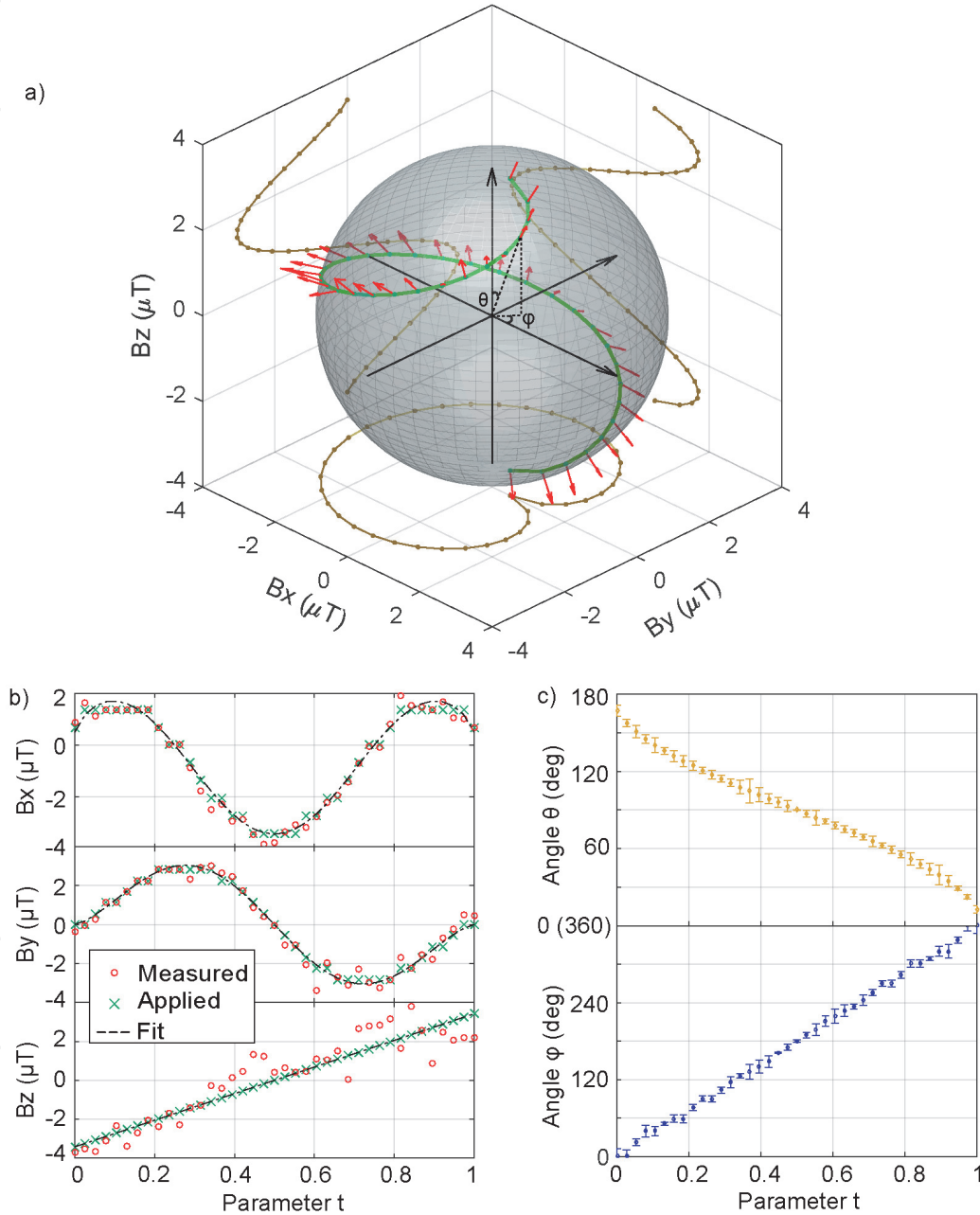


**Figure 7.**

*Demonstration of full vector sensing capability. (a) Trajectory of the detected magnetic fields using the microwave-free vector magnetometer. The green curve indicates the 3D applied field and the brown curve is the projection on  $x$ - $y$ ,  $x$ - $z$ ,  $y$ - $z$  planes. The vectors of the measured fields are indicated by red arrows. (b) the decomposed Cartesian components of both the measured (red circles) and applied (green points) magnetic fields. The applied field follows a parametric curve (black dashed lines) with  $B_x = \sqrt{|\mathbf{B}|^2 - B_z^2} \cos(2\pi t) \mu\text{T}$ ,  $B_y = \sqrt{|\mathbf{B}|^2 - B_z^2} \sin(2\pi t) \mu\text{T}$  and  $B_z = 6.82t - 3.41 \mu\text{T}$ . (c) the altitude angle (between  $\mathbf{B}$  and the  $z$ -axis)  $\theta = \arccos(B_z/|\mathbf{B}|)$  (yellow dots) and the azimuth angle (between the projection of  $\mathbf{B}$  in the  $x$ - $y$  plane and the  $x$ -axis)  $\phi = \arctan(B_y/B_x) = 2\pi t$  (blue dots) for each measured point. In the experiment, the altitude angle  $\theta$  decreases in time from  $180^\circ$  to  $0^\circ$  and the azimuth angle  $\phi$  increases from  $0^\circ$  to  $360^\circ$ . Figures adopted from Ref. [53].*



consistent with *a priori* calculations from the known coil geometry and the applied currents.

As a demonstration of full-vector sensing capacity, a set of static magnetic field vectors, whose trajectories were designed along a 3D a spiral curve on a sphere, was applied and measured. **Figure 7(a)** shows the spiral curve and the corresponding amplitudes are displayed in **Figure 7(b)**. The component in  $z$  direction is  $|B| \cos \theta$ , where  $|B|$  is the magnitude of the applied magnetic field vectors and  $\theta$  is the altitude angle (between the magnetic field to be measured and the  $z$ -axis). The  $B_x$  and  $B_y$  are  $|B| \sin \theta \cos \phi$  and  $|B| \sin \theta \sin \phi$ , respectively, where  $\phi$  is the azimuth angle (between the projection of  $\mathbf{B}$  in the  $x$ - $y$  plane and the  $x$ -axis). **Figure 7(b)** shows the corresponding values of  $B_x$  and  $B_y$ . The measured field components in  $x$  and  $y$  directions show good agreement with the amplitudes determined by *a priori* calculations. The trajectory was measured multiple times and the angles were reconstructed every time, shown in **Figure 7(c)** with the statistical error.

With the basic protocol established, this simultaneous vector magnetometry method should be extendable to single-NV probes. Single NV centers in diamond have been exploited to detect fluctuating magnetic fields (used as scalar relaxometry magnetometers) without microwaves [53, 54] as they share the spin dynamics near the GSLAC investigated above and in literature [53]. Both techniques, the present GSLAC-based vector magnetometry and relaxometry magnetometry, rely on monitoring the photoluminescence signal when the NVs are precisely turned to/near the GSLAC. Since they are operated with similar apparatus, the experimental setup for the latter can be extended for vector magnetic sensing by adding a set of 3D Helmholtz coil pairs and two LIAs. As there are no technical barriers for implementing the protocol onto a single NV center, it appears realistic to achieve nanoscale vector magnetometry applicable in a broad range of temperatures.

### 3. Zero-field magnetometry

Negatively charged NV centers in diamond have garnered wide interest as magnetometers [1, 10, 15, 25, 51, 55], with diverse applications ranging from electron spin resonance and biophysics to material science [56–62]. However, typical operation of an NV magnetometer requires an applied bias magnetic field to nonambiguously resolve magnetically sensitive features in the level structure. Due to the Zeeman effect, the bias field lifts degeneracy among the NV ground-state magnetic sublevels, allowing microwave transitions between spin states to be addressed individually [11]. Such a bias field can be detrimental for applications where it could perturb the system under examination, such as measurements in magnetically shielded environments and in magnetic susceptometry [63].

Elimination of the need for a bias field would extend the dynamic range of NV-based magnetic sensors to zero field. Zero-field NV magnetometry opens up new application avenues, and makes these versatile, solid-state sensors competitive with other magnetic field probes such as SQUIDs and alkali-vapor magnetometers [64, 65], because, despite the lower sensitivity of NVs, they offer additional benefits due to high spatial resolution and small sensor size, capability of being operated over large ranges of pressure and temperature, and wide bandwidth [1]. The relative simplicity of NVs magnetometers can readily complement existing sensors in applications such as tracking field fluctuations in experimental searches for electric dipole moments [66], zero- and ultra low-field NMR [67, 68], and magnetoencephalography or magnetocardiography [26, 69].

Magnetically sensitive microwave transitions within NV centers can be probed using the ODMR technique. At zero field, however, these transitions overlap, and shift equally with opposite sign in response to magnetic fields. Therefore, NV



ensembles have been considered unusable as zero-field magnetometers [1], except in certain cases, for detecting ac fields in the presence of applied microwaves [70].

A schematic of the experimental apparatus is described in Zheng *et al.* [71]. The ODMR traces around zero field are taken by sweeping the frequency of linear microwaves under a range of magnetic field values around zero. The ODMR acquired spectra are presented in **Figure 8(a)**, which show transitions originating from all crystal orientations, with hyperfine structure resolved for nuclear spin  $I = 1$ . These transitions are shown in detail at specific field values in **Figure 8(b)**, including at zero field, where 12 transitions overlap and merge into four distinct features.

The authors employ circularly-polarized microwaves to drive a single electron spin transition out of the feature composed of overlapping resonances. This single transition, due to Zeeman effect, has a linear dependence on the external magnetic field. The circular microwaves are generated by two, 200- $\mu\text{m}$  wires separated by a distance  $d = 4.5$  mm, printed on a circuit board that follows the design of Ref. [72]. The diamond is placed above the board with  $d/2$  distance. Each wire carries a MW signal split from the same source, with one passed through a variable phase shifter. This design and arrangement yield orthogonal oscillating magnetic fields to the  $\langle 111 \rangle$ -oriented NV centers in the diamond sample, which is verified with the high contrast between ODMR traces at certain field with  $\sigma^+$  or  $\sigma^-$  circularly-polarized microwaves (**Figure 9(a)**). The microwave field can be varied between linear and circular (**Figure 9(b)**).

**Figure 9** shows the efficacy of the circular MW polarizing. In particular, **Figure 9(b)** and (c) demonstrate a relative suppression of  $\sigma^+$  and  $\sigma^-$  transitions to below 1% of the maximum contrast, respectively. Previously overlapping transitions are thus isolated, removing the symmetric dependence as a function of the field to be measured.

It is demonstrated with a 250 pT/ $\sqrt{\text{Hz}}$  noise floor for the above NV-based zero-field magnetometer. The device employs NV ensemble in diamond with a well-

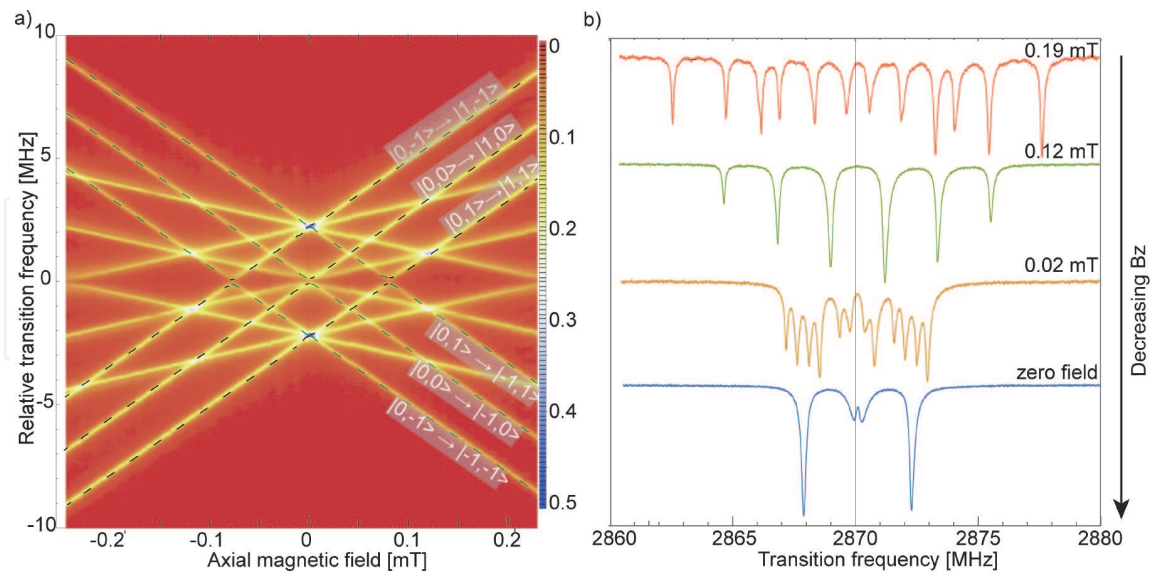


**Figure 8.**

(a) ODMR spectra with linearly polarized MWs as a function of the axial magnetic field, with transitions originating from all crystal-axis orientations. Those transitions corresponding to NVs oriented along the direction of the applied field are labeled  $(|m_s, m_I\rangle)$  and overlaid with the calculated transitions. The transitions that are not labeled are assigned to NV centers that are not oriented along the  $\langle 111 \rangle$  direction. These features overlap because they experience a common relative angle with the applied field. (b) ODMR traces for selected values of  $B_z$ . The central transitions are split at near zero field. The higher-energy peak at  $\approx 2872$  MHz are the transitions  $|m_s = 0, m_I = -1\rangle \rightarrow |m_s = +1, m_I = -1\rangle$  and  $|m_s = 0, m_I = +1\rangle \rightarrow |m_s = -1, m_I = +1\rangle$ . The lower-energy peak at  $\approx 2868$  MHz corresponds to the transitions  $|m_s = 0, m_I = +1\rangle \rightarrow |m_s = +1, m_I = +1\rangle$  and  $|m_s = 0, m_I = -1\rangle \rightarrow |m_s = -1, m_I = -1\rangle$ . Figures adopted from Ref. [71].

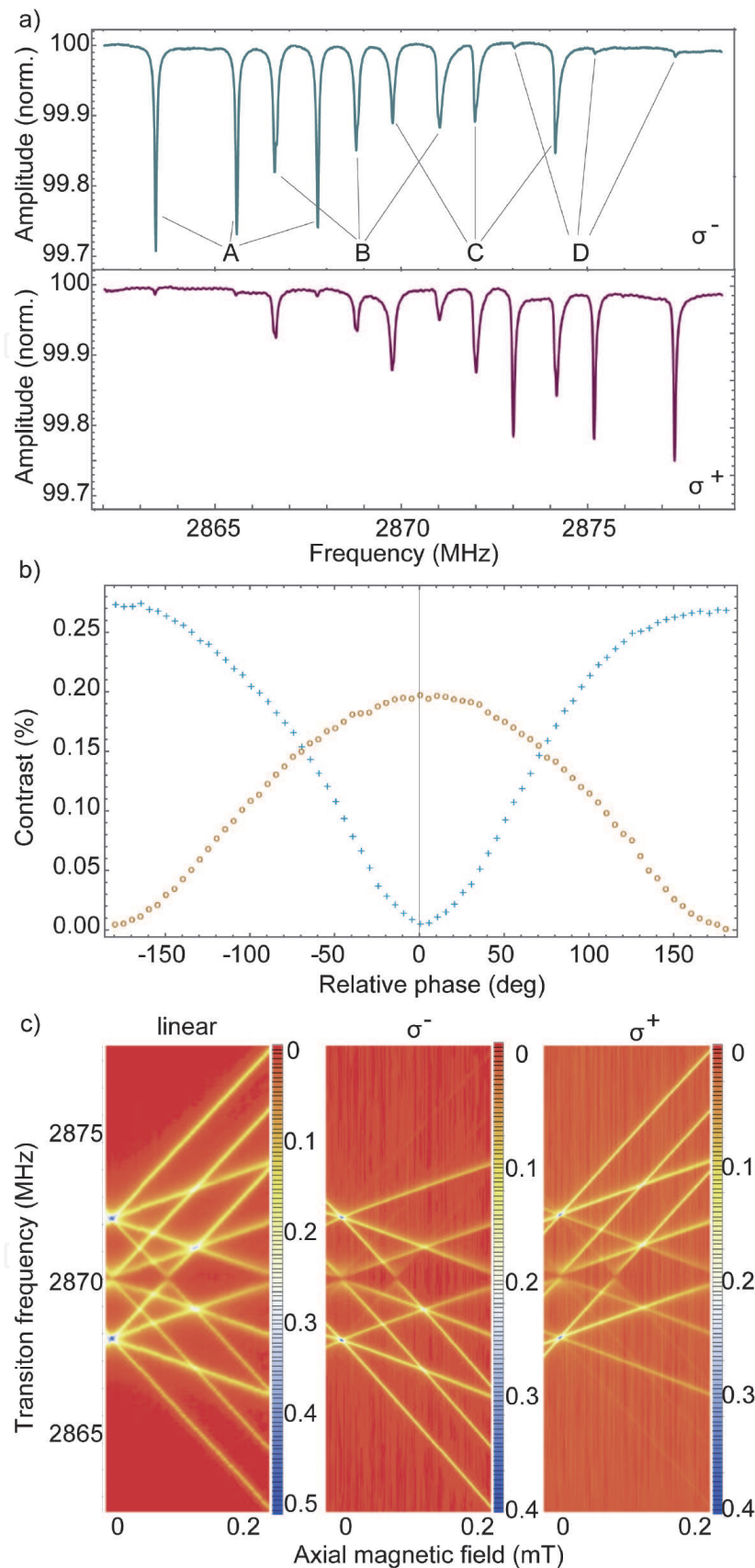


**Figure 9.**  
(a) ODMR spectrum at certain field with circularly-polarized MWs (the polarization of the applied MW is indicated at the right bottom corner of each sub-figure: Top  $\sigma^-$  and bottom  $\sigma^+$ ). The peaks are labeled into 4 groups, peaks A and D (B and C) correspond to the transitions from  $|m_s = 0\rangle$  to  $|m_s = -1\rangle$  and  $|m_s = 0\rangle$  to  $|m_s = 1\rangle$  of on-axis (off-axis) NVs, respectively. (b) Subtracted contrasts of A and D by Lorentzian fitting, as a function of the relative phase between two applied microwave fields. Blue crosses (amber circles) indicate the amplitudes of A (D). (c) ODMR traces under linear,  $\sigma^-$ ,  $\sigma^+$  MWs at various magnetic fields. The color scale indicates the peak depth, in percent, relative to the off-resonant case. Figures adopted from Ref. [71].

resolved ground-state hyperfine structure, and uses circular microwaves to selectively excite transitions between the magnetic sublevels, in the absence of such selectivity, yield ODMR signals that are first-order magnetically insensitive at near zero field. This device can find use in applications where a bias field is undesirable and extends the dynamic range of NV magnetometry to cover existing zero-field technologies such as SQUIDs and alkali-vapor magnetometers. Further improvements in the present technique will result in sensitivities that are beneficial for NMR at zero and ultra-low fields and, with further miniaturization, these zero-field diamond sensors can be useful in biomagnetic applications such as magnetocardiography and magnetoencephalography.

## **4. Outlook**

This chapter focuses on a number of novel magnetic sensing techniques with NV centers in diamond. In Section 2, a novel method for a microwave-free magnetometer based on the GSLAC, together with its utilization to achieve eddy-current imaging, is described. In addition, approaches to improve the sensitivity of the MW-free magnetometers and a different detection method—cavity-enhanced singlet-absorption measurement are discussed. In Section 3, we introduce a vector magnetometer based on the GSLAC microwave-free magnetic sensing technique, which enables simultaneous measurement of all Cartesian components of a magnetic field. In Section 4, we presented a magnetometric prototype based on ODMR which is realized with circularly polarized MWs. This magnetometer operates at zero ambient field and thus extends magnetic sensing dynamic range and opens up new application avenues. All the above magnetometers are realized in continuous-wave mode and can be potentially operated with pulse sequences.

This chapter advances in ultra-sensitive, high-bandwidth magnetometry with NV ensembles. Significant work remains to bring each to its full potential. Advances will most likely be driven by both improved pulse sequences and better materials. Additionally, the performance can be further improved with approaches such as increasing the photon collection efficiency, extending NV spin coherence times, increasing readout fidelity, and suppressing common-mode noise by differential detection and so on.

The ability to detect magnetic field patterns with high magnetic sensitivity and spatial resolution could prove a useful characterization tool in a number of fields. In particular, NV magnetometers can be used for non-invasively magnetically imaging biomagnetic systems (e.g., neurons, cardiac cells, and magnetic organs used for navigation) using microwave-free probes, vectorial stray-field imaging of magnetic structures, and detecting nuclear magnetic resonance of chemically exchanging systems at zero field [73]. The presented techniques are potentially applicable to single NV center probes, which would facilitate extraction of magnetic information with nanoscale spatial resolution and would boost numerous applications.

## **Additional information**

This chapter is based on the PhD Thesis of Huijie Zheng.

## Author details

Huijie Zheng<sup>1\*</sup>, Arne Wickenbrock<sup>1,2</sup>, Georgios Chatzidrosos<sup>1</sup>, Lykourgos Bougas<sup>1,2</sup>, Nathan Leefer<sup>1</sup>, Samer Afach<sup>1</sup>, Andrey Jarmola<sup>3</sup>, Victor M. Acosta<sup>4</sup>, Jingyan Xu<sup>5</sup>, Geoffrey Z. Iwata<sup>2</sup>, Till Lenz<sup>1</sup>, Zhiyin Sun<sup>6</sup>, Chen Zhang<sup>7</sup>, Takeshi Ohshima<sup>8</sup>, Hitoshi Sumiya<sup>9</sup>, Kazuo Nakamura<sup>10</sup>, Junichi Isoya<sup>11</sup>, Jörg Wrachtrup<sup>7</sup> and Dmitry Budker<sup>1,2,3</sup>

1 Johannes Gutenberg-Universität Mainz, Mainz, Germany

2 Helmholtz Institut Mainz, Mainz, Germany

3 Department of Physics, University of California, Berkeley, CA, USA

4 Department of Physics and Astronomy, University of New Mexico, Center for High Technology Materials, Albuquerque, NM, USA

5 Chinese Academy of Sciences, Key Lab of Quantum Information, University of Science and Technology of China, Hefei, People's Republic of China

6 Laboratory for Space Environment and Physical Sciences, Harbin Institute of Technology, Harbin, China

7 Institute of Physics, University of Stuttgart and Institute for Quantum Science and Technology IQST, Stuttgart, Germany

8 Takasaki Advanced Radiation Research Institute, National Institutes for Quantum and Radiological Science and Technology, Takasaki, Japan


9 Advanced Materials Laboratory, Sumitomo Electric Industries, Ltd., Itami, Japan

10 Application Technology Research Institute, Tokyo Gas Company, Ltd., Yokohama, Japan

11 Faculty of Pure and Applied Sciences, University of Tsukuba, Tsukuba, Japan

\*Address all correspondence to: [zheng@uni-mainz.de](mailto:zheng@uni-mainz.de)

## IntechOpen

© 2021 The Author(s). Licensee IntechOpen. This chapter is distributed under the terms of the Creative Commons Attribution License (<http://creativecommons.org/licenses/by/3.0>), which permits unrestricted use, distribution, and reproduction in any medium, provided the original work is properly cited. 



## References

- [1] L Rondin, J-P Tetienne, T Hingant, J-F Roch, P Maletinsky, and V Jacques. Magnetometry with nitrogen-vacancy defects in diamond. *Reports on Progress in Physics*, 77(5):056503, 2014.
- [2] G. Kucsko, P. C. Maurer, N. Y. Yao, M. Kubo, H. J. Noh, P. K. Lo, H. Park, and M. D. Lukin. Nanometre-scale thermometry in a living cell. *Nature Physics Letter*, 500:54–58, 2013.
- [3] V. M. Acosta, E. Bauch, M. P. Ledbetter, A. Waxman, L.-S. Bouchard, and D. Budker. Temperature dependence of the nitrogen-vacancy magnetic resonance in diamond. *Phys. Rev. Lett.*, 104:070801, 2010.
- [4] F. Dolde, H. Fedder, M. W. Doherty, T. Nobauer, F. Rempp, G. Balasubramanian, T. Wolf, F. Reinhard, L. C. L. Hollenberg, F. Jelezko, and J. Wrachtrup. Electric-field sensing using single diamond spins. *Nature Physics Letter*, 455:644–647, 2008.
- [5] Preeti Ovartchaiyapong, Kenneth W. Lee, Bryan A. Myers, Ania C. Bleszynski Jayich, A. Stacey, D. Budker, and L. C. L. Hollenberg. Dynamic strain-mediated coupling of a single diamond spin to a mechanical resonator. *Nat Commun*, 5, 2014.
- [6] M. P. Ledbetter, K. Jensen, R. Fischer, A. Jarmola, and D. Budker. Gyroscopes based on nitrogen-vacancy centers in diamond. *Phys. Rev. A*, 86: 052116, 2012.
- [7] Ashok Ajoy and Paola Cappellaro. Stable three-axis nuclear-spin gyroscope in diamond. *Phys. Rev. A*, 86:062104, 2012.
- [8] D. Maclaurin, M. W. Doherty, L. C. L. Hollenberg, and A. M. Martin. Measurable quantum geometric phase from a rotating single spin. *Phys. Rev. Lett.*, 108:240403, 2012.
- [9] Eric van Oort, Paul Stroomeer, and Max Glasbeek. Low-field optically detected magnetic resonance of a coupled triplet-doublet defect pair in diamond. *Phys. Rev. B*, 42:8605–8608, 1990.
- [10] Thomas Wolf, Philipp Neumann, Kazuo Nakamura, Hitoshi Sumiya, Takeshi Ohshima, Junichi Isoya, and Jörg Wrachtrup. Subpicotesla diamond magnetometry. *Phys. Rev. X*, 5:041001, 2015.
- [11] J. M. Taylor, P. Cappellaro, L. Childress, L. Jiang, Philipp Neumann, D. Budker, P. R. Hemmer, A. Yacoby, R. Walsworth, and M. D. Lukin. High-sensitivity diamond magnetometer with nanoscale resolution. *Nature Physics*, 4: 810–816, 2008.
- [12] VM Acosta, E Bauch, A Jarmola, LJ Zipp, MP Ledbetter, and D Budker. Broadband magnetometry by infrared-absorption detection of nitrogen-vacancy ensembles in diamond. *Applied Physics Letters*, 97(17):174104, 2010.
- [13] V. M. Acosta, A. Jarmola, E. Bauch, and D. Budker. Optical properties of the nitrogen-vacancy singlet levels in diamond. *Phys. Rev. B*, 82:201202, 2010.
- [14] Y. Dumeige, M. Chipaux, V. Jacques, F. Treussart, J.-F. Roch, T. Debuisschert, V. M. Acosta, A. Jarmola, K. Jensen, P. Kehayias, and D. Budker. Magnetometry with nitrogen-vacancy ensembles in diamond based on infrared absorption in a doubly resonant optical cavity. *Phys. Rev. B*, 87:155202, 2013.
- [15] K. Jensen, N. Leefer, A. Jarmola, Y. Dumeige, V. M. Acosta, P. Kehayias, B. Patton, and D. Budker. Cavity-enhanced room-temperature magnetometry using absorption by nitrogen-vacancy centers in diamond. *Phys. Rev. Lett.*, 112:160802, 2014.

- [16] Arne Wickenbrock, Sarunas Jurgilas, Albert Dow, Luca Marmugi, and Ferruccio Renzoni. Magnetic induction tomography using an all-optical 87rb atomic magnetometer. *Opt. Lett.*, 39(22):6367–6370, 2014.
- [17] Cameron Deans, Luca Marmugi, Sarah Hussain, and Ferruccio Renzoni. Electromagnetic induction imaging with a radio-frequency atomic magnetometer. *Applied Physics Letters*, 108(10):103503, 2016.
- [18] Arne Wickenbrock, Nathan Leefer, John W Blanchard, and Dmitry Budker. Eddy current imaging with an atomic radio-frequency magnetometer. *Applied Physics Letters*, 108(18):183507, 2016.
- [19] Georgios Chatzidrosos, Arne Wickenbrock, Lykourgos Bougas, Huijie Zheng, Oleg Tretiak, Yu Yang, and Dmitry Budker. Eddy-current imaging with nitrogen-vacancy centers in diamond. *Phys. Rev. Applied*, 11:014060, Jan 2019.
- [20] David A Simpson, Jean-Philippe Tetienne, Julia M McCoey, Kumaravelu Ganesan, Liam T Hall, Steven Petrou, Robert E Scholten, and Lloyd CL Hollenberg. Magneto-optical imaging of thin magnetic films using spins in diamond. *Scientific reports*, 6(1):1–8, 2016.
- [21] J-P Tetienne, L Rondin, P Spinicelli, M Chipaux, T Debuisschert, J-F Roch, and V Jacques. Magnetic-field-dependent photodynamics of single nv defects in diamond: an application to qualitative all-optical magnetic imaging. *New Journal of Physics*, 14(10):103033, 2012.
- [22] P. Maletinsky, S. Hong, M. S. Grinolds, B. Hausmann, M. D. Lukin, R. L. Walsworth, M. Loncar, and A. Yacoby. A robust scanning diamond sensor for nanoscale imaging with single nitrogen-vacancy centres. *Nat Nano*, 7(5):320–324, 2012.
- [23] L. Rondin, J.-P. Tetienne, P. Spinicelli, C. Dal Savio, K. Karrai, G. Dantelle, A. Thiaville, S. Rohart, J.-F. Roch, and V. Jacques. Nanoscale magnetic field mapping with a single spin scanning probe magnetometer. *Applied Physics Letters*, 100(15), 2012.
- [24] Jared H Cole and Lloyd C L Hollenberg. Scanning quantum decoherence microscopy. *Nanotechnology*, 20(49):495401, 2009.
- [25] Arne Wickenbrock, Huijie Zheng, Lykourgos Bougas, Nathan Leefer, Samer Afach, Andrey Jarmola, Victor M Acosta, and Dmitry Budker. Microwave-free magnetometry with nitrogen-vacancy centers in diamond. *Applied Physics Letters*, 109, 2016.
- [26] Riccardo Fenici, Donatella Brisinda, and Anna Maria Meloni. Clinical application of magnetocardiography. *Expert Review of Molecular Diagnostics*, 5(3):291–313, 2005.
- [27] Seiji Armstrong, Lachlan J. Rogers, Roger L. McMurtrie, and Neil B. Manson. Nv-nv electron-electron spin and nv-ns electron-electron and electron-nuclear spin interaction in diamond. *Physics Procedia*, 3(4):1569–1575, 2010.
- [28] LT Hall, P Kehayias, DA Simpson, A Jarmola, A Stacey, D Budker, and LCL Hollenberg. Detection of nanoscale electron spin resonance spectra demonstrated using nitrogen-vacancy centre probes in diamond. *Nature communications*, 7(1):1–9, 2016.
- [29] James D. A. Wood, David A. Broadway, Liam T. Hall, Alastair Stacey, David A. Simpson, Jean-Philippe Tetienne, and Lloyd C. L. Hollenberg. Wide-band nanoscale magnetic resonance spectroscopy using quantum relaxation of a single spin in diamond. *Phys. Rev. B*, 94:155402, 2016.
- [30] Ivády, Viktor and Zheng, Huijie and Wickenbrock, Arne and Bougas,

Lykourgos and Chatzidrosos, Georgios and Nakamura, Kazuo and Sumiya, Hitoshi and Ohshima, Takeshi and Isoya, Junichi and Budker, Dmitry and others. Photoluminescence at the ground state level anticrossing of the nitrogen-vacancy center in diamond. 2020:arXiv preprint arXiv:2006.05085

[31] Corey J Cochrane, Jordana Blacksberg, Mark A Anders, and Patrick M Lenahan. Vectorized magnetometer for space applications using electrical readout of atomic scale defects in silicon carbide. *Scientific Reports*, 6:37077, 2016.

[32] James Lenz and S Edelstein. Magnetic sensors and their applications. *IEEE Sensors Journal*, 6(3):631–649, 2006.

[33] D Le Sage, K Arai, DR Glenn, SJ DeVience, LM Pham, L Rahn-Lee, MD Lukin, A Yacoby, A Komeili, and RL Walsworth. Optical magnetic imaging of living cells. *Nature*, 496(7446):486–489, 2013.

[34] Matti Hämäläinen, Riitta Hari, Risto J. Ilmoniemi, Jukka Knuutila, and Olli V. Lounasmaa. Magnetoencephalography—theory, instrumentation, and applications to noninvasive studies of the working human brain. *Rev. Mod. Phys.*, 65:413–497, Apr 1993.

[35] Luong Van Su, Jeng Jen-Tzong, Lu Chih-Cheng, and Hsu Hua-Yi. Low-noise tunneling-magnetoresistance vector magnetometers with flux chopping technique. *Measurement*, 109:297–303, 2017.

[36] T. Schönau, V. Zakosarenko, M. Schmelz, R. Stolz, S. Anders, S. Linzen, M. Meyer, and H.-G. Meyer. A three-axis squid-based absolute vector magnetometer. *Review of Scientific Instruments*, 86(10):105002, 2015.

[37] S. J. Seltzer and M. V. Romalis. Unshielded three-axis vector operation

of a spin-exchange-relaxation-free atomic magnetometer. *Applied Physics Letters*, 85(20):4804–4806, 2004.

[38] B. Patton, E. Zhivun, D. C. Hovde, and D. Budker. All-optical vector atomic magnetometer. *Phys. Rev. Lett.*, 113:013001, July 2014.

[39] Georgios Chatzidrosos, Arne Wickenbrock, Lykourgos Bougas, Nathan Leefer, Teng Wu, Kasper Jensen, Yannick Dumeige, and Dmitry Budker. Miniature cavity-enhanced diamond magnetometer. *Phys. Rev. Applied*, 8:044019, Oct 2017.

[40] Y. Dumeige, M. Chipaux, V. Jacques, F. Treussart, J.-F. Roch, T. Debuisschert, V. M. Acosta, A. Jarmola, K. Jensen, P. Kehayias, and D. Budker. Magnetometry with nitrogen-vacancy ensembles in diamond based on infrared absorption in a doubly resonant optical cavity. *Phys. Rev. B*, 87:155202, Apr 2013.

[41] Cheng Gong, Lin Li, Zhenglu Li, Huiwen Ji, Alex Stern, Yang Xia, Ting Cao, Wei Bao, Chenzhe Wang, Yuan Wang, et al. Discovery of intrinsic ferromagnetism in two-dimensional van der waals crystals. *Nature*, 546(7657):265, 2017.

[42] Manuel Bonilla, Sadhu Kolekar, Yujing Ma, Horacio Coy Diaz, Vijaysankar Kalappattil, Raja Das, Tatiana Eggers, Humberto R Gutierrez, Manh-Huong Phan, and Matthias Batzill. Strong room-temperature ferromagnetism in vsc 2 monolayers on van der waals substrates. *Nature nanotechnology*, 13(4):289, 2018.

[43] Matthew Pelliccione, Alec Jenkins, Preeti Ovartchaiyapong, Christopher Reetz, Eve Emmanouilidou, Ni Ni, and Ania C Bleszynski Jayich. Scanned probe imaging of nanoscale magnetism at cryogenic temperatures with a single-spin quantum sensor. *Nature nanotechnology*, 11(8):700, 2016.



- [44] Isabell Gross, W Akhtar, V Garcia, LJ Martínez, Saddam Chouaieb, K Garcia, C Carrétéro, A Barthélémy, P Appel, P Maletinsky, et al. Real-space imaging of non-collinear antiferromagnetic order with a single-spin magnetometer. *Nature*, 549(7671): 252, 2017.
- [45] Jennifer M. Schloss, John F. Barry, Matthew J. Turner, and Ronald L. Walsworth. Simultaneous broadband vector magnetometry using solid-state spins. *Phys. Rev. Applied*, 10:034044, Sep 2018.
- [46] Chen Zhang, Heng Yuan, Ning Zhang, Lixia Xu, Jixing Zhang, Bo Li, and Jiancheng Fang. Vector magnetometer based on synchronous manipulation of nitrogen-vacancy centers in all crystal directions. *Journal of Physics D: Applied Physics*, 51(15): 155102, 2018.
- [47] Yi-Xiang Liu, Ashok Ajoy, and Paola Cappellaro. Nanoscale vector dc magnetometry via ancilla-assisted frequency up-conversion. *Phys. Rev. Lett.*, 122:100501, Mar 2019.
- [48] Pengfei Wang, Zhenheng Yuan, Pu Huang, Xing Rong, Mengqi Wang, Xi-angkun Xu, Changkui Duan, Chenyong Ju, Fazhan Shi, and Jiangfeng Du. High-resolution vector microwave magnetometry based on solid-state spins in diamond. *Nature communications*, 6(1):1–5, 2015.
- [49] Lucas Thiel, Zhe Wang, Märta A Tschudin, Dominik Rohner, Ignacio Gutiérrez-Lezama, Nicolas Ubrig, Marco Gibertini, Enrico Giannini, Alberto F Morpurgo, and Patrick Maletinsky. Probing magnetism in 2d materials at the nanoscale with single-spin microscopy. *Science*, 364(6444): 973–976, 2019.
- [50] Huijie Zheng, Zhiyin Sun, Georgios Chatzidrosos, Chen Zhang, Kazuo Nakamura, Hitoshi Sumiya, Takeshi Ohshima, Junichi Isoya, Jörg Wrachtrup, Arne Wickenbrock, and Dmitry Budker. Microwave-free vector magnetometry with nitrogen-vacancy centers along a single axis in diamond. *Phys. Rev. Applied*, 13:044023, Apr 2020.
- [51] Huijie Zheng, Georgios Chatzidrosos, Arne Wickenbrock, Lykourgos Bougas, Reinis Lazda, Andris Berzins, Florian Helmuth Gahbauer, Marcis Auzinsh, Ruvin Ferbe, and Dmitry Budker. Level anti-crossing magnetometry with color centers in diamond. *Proc. of SPIE*, page 101190X, Feb 2017.
- [52] R. J. Epstein, F. M. Mendoza, Y. K. Kato, and D. D. Awschalom. Anisotropic interactions of a single spin and dark-spin spectroscopy in diamond. *Nature Physics*, 1:94–98, 2005.
- [53] David A. Broadway, James D. A. Wood, Liam T. Hall, Alastair Stacey, Matthew Markham, David A. Simpson, Jean-Philippe Tetienne, and Lloyd C. L. Hollenberg. Anticrossing spin dynamics of diamond nitrogen-vacancy centers and all-optical low-frequency magnetometry. *Phys. Rev. Applied*, 6: 064001, Dec 2016.
- [54] James DA Wood, Jean-Philippe Tetienne, David A Broadway, Liam T Hall, David A Simpson, Alastair Stacey, and Lloyd CL Hollenberg. Microwave-free nuclear magnetic resonance at molecular scales. *Nature communications*, 8(1):1–6, 2017.
- [55] Aharon Blank, Guy Shapiro, Ran Fischer, Paz London, and David Gershoni. Optically detected magnetic resonance imaging. *Applied Physics Letters*, 106(3):034102, 2015.
- [56] Gopalakrishnan Balasubramanian, IY Chan, Roman Kolesov, Mohannad Al-Hmoud, Julia Tisler, Chang Shin, Changdong Kim, Aleksander Wojcik, Philip R Hemmer, Anke Krueger, et al. Nanoscale imaging magnetometry with



diamond spins under ambient conditions. *Nature*, 455(7213):648, 2008.

[57] F. Jelezko and J. Wrachtrup. Single defect centres in diamond: A review. *physical status solidi (a)*, 203(13):3207–3225, 2006.

[58] F Kong, P.J Zhao, X.Y. Ye, Z.C Wang, Z.Y Qin, P. Yu, J.H. Su, F.Z. Shi, and J.F. Du. Nanoscale zero-field electron spin resonance spectroscopy. *Nature Communications*, 9:1563, Apr 2018.

[59] John F. Barry, Matthew J. Turner, Jennifer M. Schloss, David R. Glenn, Yuyu Song, Mikhail D. Lukin, Hongkun Park, and Ronald L. Walsworth. Optical magnetic detection of single-neuron action potentials using quantum defects in diamond. *Proceedings of the National Academy of Sciences*, 113(49):14133–14138, 2016.

[60] Steffen Steinert, Florian Dolde, Philipp Neumann, Andrew Aird, Boris Naydenov, Gopalakrishnan Balasubramanian, Fedor Jelezko, and Joerg Wrachtrup. High sensitivity magnetic imaging using an array of spins in diamond. *Review of scientific instruments*, 81(4):043705, 2010.

[61] C. L. Degen. Scanning magnetic field microscope with a diamond single spin sensor. *Applied Physics Letters*, 92(24):243111, 2008.

[62] P. London, J. Scheuer, J.-M. Cai, I. Schwarz, A. Retzker, M. B. Plenio, M. Katagiri, T. Teraji, S. Koizumi, J. Isoya, R. Fischer, L. P. McGuinness, B. Naydenov, and F. Jelezko. Detecting and polarizing nuclear spins with double resonance on a single electron spin. *Phys. Rev. Lett.*, 111:067601, Aug 2013.

[63] D. Eberbeck, A. P. Astalan, K. Petersson, F. Wiekhorst, C. Bergemann, C. Johansson, U. Steinhoff, H. Richter, A. Krozer, and L. Trahms. Ac susceptometry and magnetorelaxometry

for magnetic nanoparticle based biomolecule detection. In Jos Vander Sloten, Pascal Verdonck, Marc Nyssen, and Jens Haueisen, editors, *4th European Conference of the International Federation for Medical and Biological Engineering*, pages 2317–2321, Berlin, Heidelberg, 2009. Springer Berlin Heidelberg.

[64] Guzhi Bao, Arne Wickenbrock, Simon Rochester, Weiping Zhang, and Dmitry Budker. Suppression of the nonlinear zeeman effect and heading error in earth-field-range alkali-vapor magnetometers. *Phys. Rev. Lett.*, 120: 033202, Jan 2018.

[65] Wei Quan, Kai Wei, and Hairong Li. Precision measurement of magnetic field based on the transient process in a k-rb-21ne co-magnetometer. *Opt. Express*, 25(8):8470–8483, Apr 2017.

[66] G. Bison, V. Bondar, P. Schmidt-Wellenburg, A. Schnabel, and J. Voigt. Sensitive and stable vector magnetometer for operation in zero and finite fields. *Opt. Express*, 26(13):17350–17359, Jun 2018.

[67] Min Jiang, Teng Wu, John W. Blanchard, Guanru Feng, Xinhua Peng, and Dmitry Budker. Experimental benchmarking of quantum control in zero-field nuclear magnetic resonance. *Science Advances*, 4(6), 2018.

[68] M. P. Ledbetter, I. M. Savukov, D. Budker, V. Shah, S. Knappe, J. Kitching, D.J. Michalak, S. Xu, and A. Pines. Zero-field remote detection of nmr with a microfabricated atomic magnetometer. *Proceedings of the National Academy of Sciences of the United States of America*, 105(7):2286–2290, 2008.

[69] A I Ahonen, M S Hamalainen, M J Kajola, J E T Knuutila, P P Laine, O V Lounasmaa, L T Parkkonen, J T Simola, and C D Tesche. 122-channel squid instrument for investigating the magnetic signals from the human brain. *Physica Scripta*, 1993(T49A):198, 1993.

[70] Soya Saijo, Yuichiro Matsuzaki, Shiro Saito, Tatsuma Yamaguchi, Ikuya Hanano, Hideyuki Watanabe, Norikazu Mizuochi, and Junko Ishi-Hayase. Ac magnetic field sensing using continuous-wave optically detected magnetic resonance of nitrogen-vacancy centers in diamond. *Applied Physics Letters*, 113(8):082405, 2018.

[71] Huijie Zheng, Jingyan Xu, Geoffrey Z. Iwata, Till Lenz, Julia Michl, Boris Yavkin, Kazuo Nakamura, Hitoshi Sumiya, Takeshi Ohshima, Junichi Isoya, Jörg Wrachtrup, Arne Wickenbrock, and Dmitry Budker. Zero-field magnetometry based on nitrogen-vacancy ensembles in diamond. *Phys. Rev. Applied*, 11:064068, Jun 2019.

[72] M. Mrozek, J. Mlynarczyk, D. S. Rudnicki, and W. Gawlik. Circularly polarized microwaves for magnetic resonance study in the ghz range: Application to nitrogen-vacancy in diamonds. *Applied Physics Letters*, 107(1):013505, 2015.

[73] Danila A Barskiy, Michael CD Tayler, Irene Marco-Rius, John Kurhanewicz, Daniel B Vigneron, Sevil Cikrikci, Ayca Aydogdu, Moritz Reh, Andrey N Pravdivtsev, Jan-Bernd Hövener, et al. Zero-field nuclear magnetic resonance of chemically exchanging systems. *Nature communications*, 10(1):1–9, 2019.